JACS
JOURNAL OF THE AMERICAN CHEMICAL SOCIETY

Article

pubs.acs.org/JACS

Preparation of Tantalum-Based Oxynitride Nanosheets by Exfoliation of a Layered Oxynitride, $CsCa_2Ta_3O_{10-x}N_y$, and Their Photocatalytic Activity

Shintaro Ida,*[†,‡,§] Yohei Okamoto,[†] Maki Matsuka,[†,‡] Hidehisa Hagiwara,[†,‡] and Tatsumi Ishihara[†,‡]

[†]Department of Applied Chemistry, Faculty of Engineering, Kyushu University, 744 Motooka, Nishi-ku, Fukuoka 819-0395, Japan,

[‡]International Institute for Carbon Neutral Energy Research (I2CNER), Kyushu University, Motooka 744, Nishi-ku, Fukuoka 819-0395, Japan,

[§]PRESTO, Japan Science and Technology Agency (JST)4-1-8, Honcho Kawaguchi, Saitama 332-0012, Japan

Supporting Information

ABSTRACT: Calcium tantalum oxynitride $[Ca_2Ta_3O_{9.7}N_{0.2}]^-$ nanosheets were prepared by exfoliating a layered perovskite oxynitride ($CsCa_2Ta_3O_{9.7}N_{0.2}$) via proton exchange and two-step intercalation of ethylamine and tetrabutylammonium ions. Monolayer nanosheet was prepared by the above processes, although some bilayer or trilayer nanosheets were also produced. The $[Ca_2Ta_3O_{9.7}N_{0.2}]^-$ nanosheets exhibited photocatalytic activity for H_2 evolution from water under visible light irradiation. In contrast, $CsCa_2Ta_3O_{9.7}N_{0.2}$ exhibited very low photocatalytic activity for H_2 evolution under the visible light irradiation, even when methanol was added to water as a sacrificial agent. The improved photocatalytic activity originates from the characteristics of nanosheets such as their molecular thickness and large surface area. Further, the Rh-loaded $[Ca_2Ta_3O_{9.7}N_{0.2}]^-$ nanosheets restacked with protons exhibited photocatalytic activity for H_2 and O_2 evolution from pure water under UV-light irradiation. The ratio of H_2/O_2 evolved was around 3. The ratio of N/O in the catalyst remained the same after the photocatalytic reaction, signifying that there was no decomposition of the catalyst during the reaction. This indicates that the present N-doped nanosheet is stable in the photocatalytic reaction.

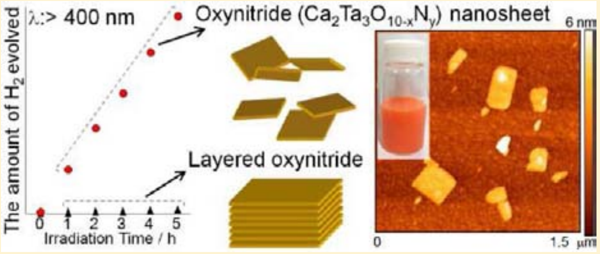

INTRODUCTION

Two-dimensional nanocrystals (nanosheets) prepared by exfoliation of layered parent materials are single crystals with thicknesses on the order of molecular sizes. Nanosheets are about 0.5−2.0-nm thick depending on the parent layered material, while their lateral dimensions range from several hundred nanometers to several micrometers.[1−15] Nanosheets with such unique structures have various potential applications. For example, oxide,[1−10] hydroxide,[11−14] and graphene nanosheets[15] have been investigated for various potential applications including fillers,[16] cosmetics,[17] ultraviolet protection films, and high-speed transistors.[18] However, only a few studies have investigated the preparation and application of oxynitride nanosheets.[19,20]

Oxynitrides have been studied for various applications including photocatalytic hydrogen production,[21−24] dielectric materials with ultrahigh dielectric properties,[25,26] and electrode catalysts for polymer electrode fuel cells (PEFCs).[27] In particular, tantalum-based oxynitrides such as TaON, $ATaO_2N$ (A = Ca, Sr, Ba), and layered oxynitrides have been investigated as potential visible-light photocatalysts.[22−24] A high crystallinity and a large surface area are critical for realizing high-efficiency photocatalysts, nanosheets satisfy both of these requirements. In addition, the molecular size thickness of nanosheets also improves their quantum efficiency. For conventional powder catalysts with particle diameters in the range 0.5−3.0 μm, photoexcited electrons and holes generated within them have to travel a long distance to the surface to react with water. However, electrons and holes may recombine or become trapped at defect sites during this long trip to the surface, which can reduce their hydrogen production efficiency. However, photoexcited electrons and holes generated in a nanosheet can reach its surface without encountering obstructions due to its ultrathin thickness and high crystallinity. For example, $[Nb_6O_{17}]^{4-}$ and $[Ca_2Nb_3O_{10}]^-$ nanosheets have been reported to have higher catalytic efficiencies than their parent compounds.[28−33] Unfortunately, these nanosheets have large band gaps and are thus not active under visible light irradiation. As mentioned above, other studies of oxynitrides have investigated the ultrahigh dielectric constants of $BaTaO_2N$ and $SrTaO_2N$[25,26] and a novel metal-free cathode catalyst for PEFCs using TaON.[27] In these studies, a high crystallinity and a large surface area are vital for reducing the leakage current or improving the catalytic activity.

Received: May 5, 2012
Published: August 28, 2012

dx.doi.org/10.1021/ja3043678 | J. Am. Chem. Soc. 2012, 134, 15773−15782

Thus, tantalum-based oxynitride nanosheets have the potential to realize advances in photocatalysts, dielectric materials, and PEFCs. To date, nitrogen-doped titania and niobate nanosheets have been investigated.[19,20] However, there have been no reports on tantalum-based oxynitride nanosheets, possibly due to the difficulty in intercalating tetrabutylammonium (TBA^+) ions (an exfoliation reagent) into tantalum-based layered oxynitrides such as $HCa_2Ta_3O_{10-x}N_y$ and $HSr_2Ta_3O_{10-x}N_y$. Our preliminary experiments confirmed that TBA^+ ions could not be directly intercalated into $HCa_2Ta_3O_{10-x}N_y$.

Therefore, this study reports a successful example of the preparation of tantalum-based oxynitride nanosheets ($Ca_2Ta_3O_{10-x}N_y$) from the parent layered perovskite oxynitride ($CsCa_2Ta_3O_{10-x}N_y$) based on a two-step intercalation process. Their photocatalytic activity for hydrogen production from water was investigated under visible light irradiation as one example of an application of oxynitride nanosheets.

EXPERIMENTAL SECTION

Nanosheet Preparation. Calcium tantalum oxynitride nanosheets were prepared from the layered oxide, $CsCa_2Ta_3O_{10}$. The parent layered oxide was prepared from $CsCO_3$ (95.0% Wako), $Ca(OOCCH_3)_2 \cdot H_2O$ (99.0% Wako), and Ta_2O_5 (99.9% Wako) according to the literature.[24] The mixture of these reagents was calcinated at 1000 °C for 10 h. An excess of alkali metal carbonate (50 mol.%) was added to compensate for the loss due to volatilization of the alkali component. The parent layered oxide prepared was converted into the layered oxynitride, $CsCa_2Ta_3O_{10-x}N_y$ by calcination at 800 °C under NH_3 flow (100 mL/min) for 6 h. The Cs ions in the layered oxynitride were exchanged with protons by acid exchange with 3 M HCl solution for a week. After proton exchange, the powder was washed in several changes of water by centrifugation. The protonated form (1.0 g) was stirred in 100 mL of a 1.0 M ethylamine (EA) aqueous solution to intercalate the EA into the interlayer for 5 days. The EA-intercalated layered oxynitride (1.0 g) was stirred for one week in 150 mL of a 0.025 M tetrabutylammonium hydroxide (TBAOH) aqueous solution to exfoliate into nanosheets. The separation of unexfoliated power was performed by spontaneous precipitation for 1 day and the supernatant was used as a nanosheet suspension. The nanosheet concentration was calculated from the powder obtained by drying the nanosheet suspension at 500 °C. The nanosheet suspension had a concentration of about 2.0 g/L.

Photocatalytic Reactions. A photocatalytic reaction was performed using a conventional closed circulation system (see the Supporting Information, SI). A quartz reaction cell was irradiated by light from an external light source. During the reaction, the suspension was mixed using a magnetic stirring bar. Ar gas (initial pressure: 18.3 kPa) was used as the circulating carrier gas. The amounts of H_2 and O_2 formed were measured by gas chromatography, which was connected to a conventional volumetric circulating line by a vacuum pump. 200 mL of water, 0.1 M $AgNO_3$ aqueous solution, or 20 vol.% methanol aqueous solution was used as the reaction solution. The amounts of catalyst were 200 or 10 mg. Co-catalysts were photodeposited on nanosheets in 20 vol.% methanol aqueous solution (100 mL of nanosheet suspension, 40 mL of methanol, 30 mL of water) containing $RhCl_3 \cdot 3H_2O$ (99.5%, Wako), $Ru(NH_4)_2Cl_6$ (Wako), or $Pt(NH_3)_4(NO_3)_2$ (99.995%, Aldrich) by irradiation with the 500 W Xe lamp for 12 h. The loading amount was adjusted by changing the amount of $RhCl_3 \cdot 3H_2O$, $Ru(NH_4)_2Cl_6$, and $Pt(NH_3)_4(NO_3)_2$ aqueous solutions. After loading the cocatalyst, a cellophane tube filled with 0.01 M H_2SO_4 aqueous solution was immersed in the nanosheet suspension while stirring constantly. This resulted in nanosheet deposition due to proton absorption. The deposited nanosheets were washed in several changes of water by centrifugation to remove residual TBAOH. The nanosheet paste obtained by centrifugation was used without drying for photocatalytic activity evaluations. In the case of the photocatalytic hydrogen evolution test from methanol aqueous solution, the photocatalytic activity was evaluated using the nanosheet suspension used for loading the cocatalyst without any change.

Characterization and Equipment. The crystal structure was analyzed by X-ray powder diffraction (Cu Kα radiation; Rigaku, RINT-2500). The oxygen-to-nitrogen ratio was determined by a HNO analyzer (Horiba, EMGA-930). Thermogravimetric differential thermal analysis was performed using a thermal analyzer (Rigaku, 8120). The surface morphologies of the powders were analyzed by scanning electron microscopy (SEM; JEOL, SU8000) and digital microscopy (Keyence, VH-Z500R). UV−vis absorption spectra were obtained by a reflection method using a spectrophotometer (HITACHI U-3310) with an integrating sphere. Five faces except for the entrance face of light of a rectangular quartz cell, with a light path length of 1 mm, were covered with reflectors to minimize the scattering effect. Raman spectroscopy was carried out using a Horiba Jobin Yvon HR800 with 744 nm initial excitation laser. The total optical modes of Raman spectrum of $CsCa_2Ta_3O_{10}$ was determined bansed on the information provided by the Bilbao Crystallographic Center Web site (www.cryst.ehu.es). The thickness of the exfoliated nanosheets was measured by atomic force microscopy (AFM) (Seiko, Nanocute). Transmission electron microscopy (TEM), high-angle annular dark-field scanning transmission electron microscopy (HAADF-STEM) images, and selective-area electron diffraction (SAED) pattern of nanosheets were obtained using JEOL JEM2400 and JEM-ARM200F microscopes. ^1H magic-angle spinning (MAS) nuclear magnetic resonance (NMR) spectra were obtained using a Bruker MSL400 spectrometer. The sample spinning rate was 30 or 8 kHz and adamantane was used as the reference material. The H_2, O_2, N_2, and CH_4 gases generated in the photocatalytic reaction were measured by a gas chromatography with a thermal conductivity detector (Shimadzu Corp., GC-8A). The CH_3COO^- and $HCOO^-$ ions formed in the photocatalytic reaction were measured by ion chromatography (DIONEX, ICS-1000). A 500 W Xe lamp (USHIO, SX-UI500XQ) and 300 W Xe lamp (ASAHI SPECTRA, MAX-302) were used as light sources for the photocatalytic reaction.

RESULTS AND DISCUSSION

The first step in the synthesis of $Ca_2Ta_3O_{10-x}N_y$ nanosheets was the nitridation of $CsCa_2Ta_3O_{10}$ to $CsCa_2Ta_3O_{10-x}N_y$. Figure 1a,b show XRD patterns of $CsCa_2Ta_3O_{10}$ and $CsCa_2Ta_3O_{10-x}N_y$, respectively. $CsCa_2Ta_3O_{10}$ and $CsCa_2Ta_3O_{10-x}N_y$ both have tetragonal symmetry with P4/*mmm* space group ($a = 0.38672$ nm; $c = 1.55323$ nm).[34] The *a*-axis was slightly longer ($a = 0.38683$ nm) after nitridation, as shown in Figure 1a,b. There were no other significant differences in the diffraction patterns of the layered oxide and oxynitride, which agrees with the result reported previously.[24]

This indicates that nitrogen partially substituted oxygen in the layered oxide without altering the crystal phase. Nitrogen and oxygen have valencies of −3 and −2, respectively; this implies that three oxygen atoms are substituted by two nitrogen atoms to compensate the charge. TG/DTA analysis of $CsCa_2Ta_3O_{10-x}N_y$ in 20−800 °C in ambient air revealed that the total weight increased by 0.389% due to nitrogen replacing oxygen (Figure 2). The N/O molar ratio of $CsCa_2Ta_3O_{10-x}N_y$ was determined by the HNO analyzer to be approximately 2% ($CsCa_2Ta_3O_{9.7}N_{0.2}$). Figure 1c shows the XRD pattern of protonated layered oxynitride ($H-Ca_2Ta_3O_{10-x}N_y$). The Cs atoms in $CsCa_2Ta_3O_{9.7}N_{0.2}$ were exchanged with protons by the acid treatment. The N/O molar ratio of $H-Ca_2Ta_3O_{10-x}N_y$ was determined to be approximately 2% ($H-Ca_2Ta_3O_{9.7}N_{0.2}$). The phase crystallographic structure of $H-Ca_2Ta_3O_{9.7}N_{0.2}$ differs from those of its parent compounds due to the space group changing from P4/*mmm* to I4/*mmm*. The protonated form was stirred in ethylamine (EA) aqueous solution to intercalate the

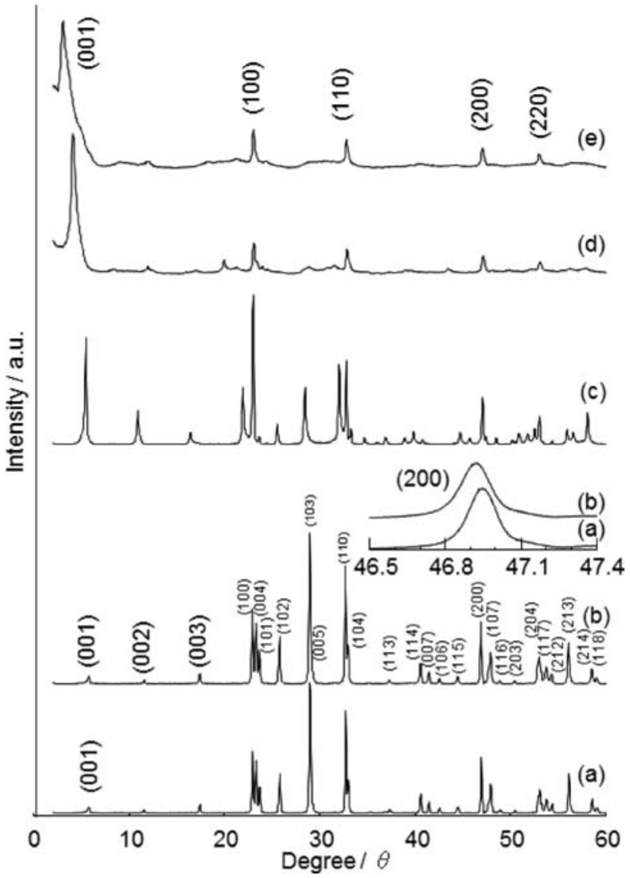

Figure 1. XRD pattern of (a) $CsCa_2Ta_3O_{10}$, (b) $CsCa_2Ta_3O_{10-x}N_y$, (c) $HCa_2Ta_3O_{10-x}N_y$, (d) EA-intercalated $Ca_2Ta_3O_{10-x}N_y$, and (e) $Ca_2Ta_3O_{10-x}N_y$ nanosheet powder.

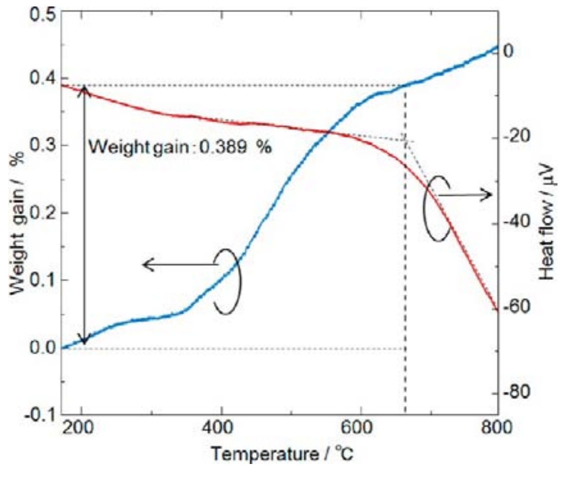

Figure 2. TG/DTA curve of $CsCa_2Ta_3O_{10-x}N_y$ in ambient air.

EA into the interlayer. XRD pattern of the EA-intercalated $Ca_2Ta_3O_{9.7}N_{0.2}$ indicates that the distance between layers in the H−$Ca_2Ta_3O_{9.7}N_{0.2}$ system increased due to EA intercalation as indicated by the diffraction peak of the (00*l*) plane being detected at a lower angle (Figure 1d). The basal distance of the EA-intercalated form was 2.209 nm. The diffraction peaks assigned to the (00*l*) and (*hk*0) planes were detected in EA−$Ca_2Ta_3O_{9.7}N_{0.2}$, whereas no diffraction peak was observed for the (*hkl*) plane indicating that the layered system became slightly disordered on EA intercalation.

The $[Ca_2Ta_3O_{9.7}N_{0.2}]^-$ nanosheets were synthesized by stirring EA−$Ca_2Ta_3O_{9.7}N_{0.2}$ in TBAOH aqueous solution. During synthesis, the layered structure exfoliates into nanosheets though the intercalation of bulky TBA^+ ions into interlayers. Figure 1e shows XRD patterns of the $Ca_2Ta_3O_{9.7}N_{0.2}$ nanosheet powder obtained by centrifuging the $Ca_2Ta_3O_{9.7}N_{0.2}$ nanosheet suspension. The peaks of the (001) plane shifted to even lower angles due to the presence of TBA^+ ions in the interlayers to compensate the individual negatively charged nanosheets. The basal distance of the nanosheet powder was 2.995 nm.

It is interesting to note that $Ca_2Ta_3O_{9.7}N_{0.2}$ nanosheets could not be fabricated directly from H−$Ca_2Ta_3O_{9.7}N_{0.2}$, since TBA^+ ions are not intercalated into H− $Ca_2Ta_3O_{9.7}N_{0.2}$ without the EA intercalation step (see SI Figure S2). This strongly suggests that EA intercalation is an essential step in the nanosheet synthesis. The process of intercalation of amine into H−$Ca_2Ta_3O_{9.7}N_{0.2}$ is commonly understood as an acid−base reaction between interlayer protons (Brønsted acid) and amines (Brønsted base). This process generally depends on the size and charge density of the guest species, and the hydration state of the layered compounds. A TBA^+ ion is a quaternary ammonium ion with four butyl groups attached to a positively charged nitrogen atom at the center. The diameter of a TBA^+ ion is 0.8 nm which is larger than the interlayer distance of H−$Ca_2Ta_3O_{9.7}N_{0.2}$ (around 0.2 nm). This relatively large diameter of TBA^+ ion may have been one of the possible reasons for the current finding. Further, it was found that drying of H− $Ca_2Ta_3O_{9.7}N_{0.2}$ is also a crucial stage in the fabrication of $Ca_2Ta_3O_{9.7}N_{0.2}$ nanosheets. When H−$Ca_2Ta_3O_{9.7}N_{0.2}$ was dried at 100 °C, EA intercalation was not fully completed, indicating that the hydration state of H−$Ca_2Ta_3O_{9.7}N_{0.2}$ affects the intercalation reaction. The optimum drying temperature for EA intercalation of H−$Ca_2Ta_3O_{9.7}N_{0.2}$ was found to be around room temperature, preventing hydrated water from evaporating from the interlayers. As to be described in a later section, the state of protons in the interlayer of H−$Ca_2Ta_3O_{9.7}N_{0.2}$ was affected by the drying condition. Thus, the hydration state of the layered compounds and the large diameter of TBA^+ ion discussed earlier may have necessitated the two-step intercalation for the present experimental conditions.

Figure 3a−f shows the physical appearance, optical microscopy, and SEM images of the parent compounds before ($CsCa_2Ta_3O_{10}$) and after ($CsCa_2Ta_3O_{9.7}N_{0.2}$) calcination in a NH_3 atmosphere (nitridation). The optical microscopy and SEM images (Figure 3c−f) were taken at the same position before and after nitridation. The color of the powder changed from white to orange, while the crystal shapes remained the same. This indicates that this nitriding reaction proceeded without large changes in the crystal structure. The powder consisted of flat or cubic crystals with grain sizes of about 0.1−0.5 μm. The slight color difference between Figure 3, parts b and d, may be due to the CCD camera filters used.

The position of nitrogen in the $Ca_2Ta_3O_{9.7}N_{0.2}$ nanosheets was investigated by ^1H NMR. Figure 4a,b shows ^1H MAS NMR spectra of protonated layered oxide (without nitridation, H−$Ca_2Ta_3O_{10}$) and protonated layered oxynitride (H−$Ca_2Ta_3O_{9.7}N_{0.2}$) dried in vacuum at 120 °C, respectively. There are three peaks at 1.07, 6.23, and 12.23 ppm in H−$Ca_2Ta_3O_{10}$, whereas the spectrum for H−$Ca_2Ta_3O_{9.7}N_{0.2}$ contains five peaks at 1.08, 4.30, 6.65, 9.90, and 12.05 ppm. This indicates that there are more differently bonded hydrogens

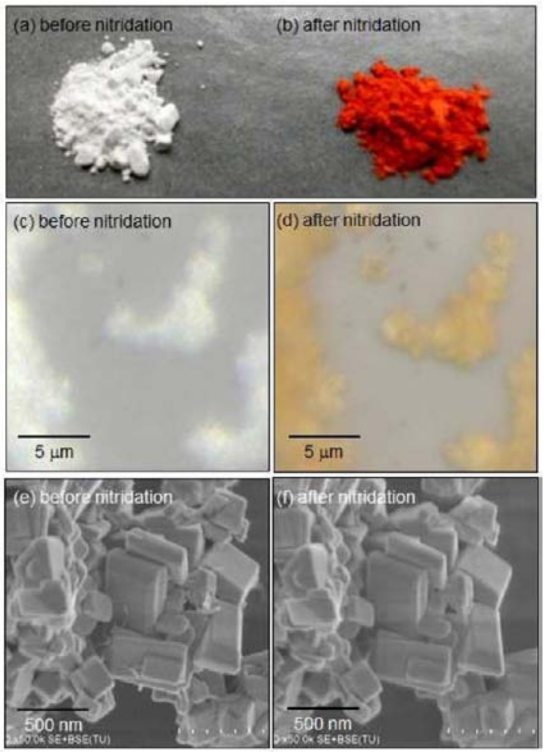

Figure 3. The physical appearance (a), (b), optical microscopy (c), (d), and SEM (e), (f) images of the sample powder before ($CsCa_2Ta_3O_{10}$) and after ($CsCa_2Ta_3O_{9.7}N_{0.2}$) calcination in a NH_3 atmosphere at 800 °C.

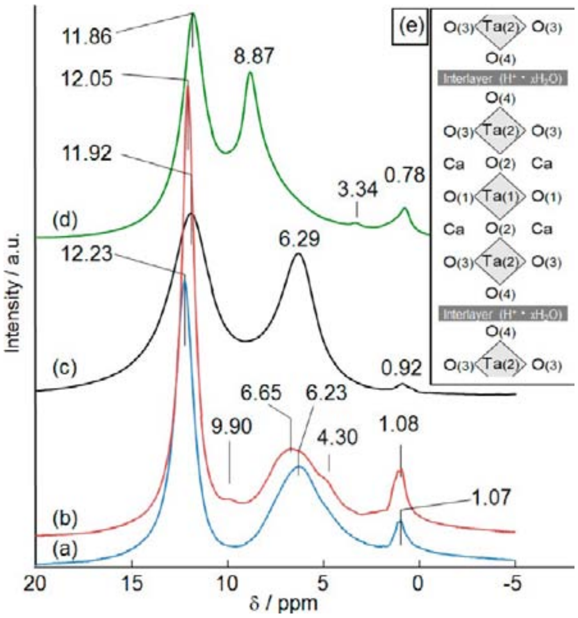

Figure 4. ^1H MAS NMR spectra for (a) $H{-}Ca_2Ta_3O_{10}$ (30 kHz) and (b) $H{-}Ca_2Ta_3O_{9.7}N_{0.2}$ (30 kHz) after removal of adsorbed and/or intercalated water by drying in vacuum at 120 °C, (c) $HCa_2Ta_3O_{10}{\cdot}xH_2O$ (8 kHz) and (d) $H{-}Ca_2Ta_3O_{9.7}N_{0.2}{\cdot}xH_2O$ (8 kHz) after drying at room temperature. (f) The structural model of $H{-}Ca_2Ta_3O_{10}$.

in $H{-}Ca_2Ta_3O_{9.7}N_{0.2}$ than in $H{-}Ca_2Ta_3O_{10}$. Regarding the assignment of the above peaks, a similar result has been reported for $HSr_2Nb_3O_{10}$, which has a similar structure as $HCa_2Ta_3O_{10}$.[35] $HSr_2Nb_3O_{10}$ has two peaks at 1.3 and 10.0 ppm; the peak at 1.3 ppm is assigned to isolated Nb−OH groups without hydrogen bonds, while the peak at 10.0 ppm is due to strongly acidic OH groups fixed in the interlayer space. In the present study, the peaks at about 1 and 12 ppm of $HCa_2Ta_3O_{10}$ and $H{-}Ca_2Ta_3O_{9.7}N_{0.2}$ are assignable to the isolated Ta−OH group without hydrogen bonds and strongly acidic OH groups fixed in the interlayer. The peaks around 6−7 ppm for a layered compound containing transition metal octahedra such as TiO_6, NbO_6, and TaO_6 are reported to be attributed to hydrogen-bonded M−OH (M: Ti, Nb, Ta).[36] On the basis of previously reported results, the present peaks at 6.23 and 6.65 ppm for $HCa_2Ta_3O_{10}$ and $H{-}Ca_2Ta_3O_{9.7}N_{0.2}$ can be similarly assigned to hydrogen-bonded Ta−OH. The other small peaks (4.30 and 9.90 ppm) of $H{-}Ca_2Ta_3O_{9.7}N_{0.2}$ indicate that there are two nitrogen doping sites that can be in contact with protons in the interlayer. One is the top oxygen site (Ta(2)−O(4)) in TaO_6 octahedra and the other one is the middle oxygen site (Ta(2)−O(3)−Ta(2)) between TaO_6 octahedra, as shown in the structural model of Figure 4e. The ^1H NMR peaks assigned to $Ta{-}NH_2$ and Ta═NH in Ta(V) amido imido complex appear around 4 and 9 ppm, respectively.[37] Therefore, the new peaks at 4.30 and 9.90 ppm of $H{-}Ca_2Ta_3O_{9.7}N_{0.2}$ may be due to $Ta(2){-}NH_2$ and Ta(2)−(NH)−Ta(2), respectively. These results indicate that nitrogen in the host layer is present in at least two oxygen sites (O(4) and O(3) sites).

Figure 4c,d shows the ^1H MAS NMR spectra of hydrated protonated layered oxide and oxynitride ($H{-}Ca_2Ta_3O_{10}{\cdot}xH_2O$ and $H{-}Ca_2Ta_3O_{9.7}N_{0.2}{\cdot}xH_2O$), respectively. The peaks at about 1 (0.92 and 0.78) and 12 (12.23 and11.86) ppm are assignable to the isolated Ta−OH group without hydrogen bonds and strongly acidic OH groups fixed in the interlayer. The peaks at 6.29 and 8.87 ppm of $H{-}Ca_2Ta_3O_{10}{\cdot}xH_2O$ and $H{-}Ca_2Ta_3O_{9.7}N_{0.2}{\cdot}xH_2O$ were shifted to lower ppm (6.23 and 6.65 ppm, respectively) by the drying treatment. Therefore, these bonding conditions might be related to free water intercalated into the interlayer. Presumably, these peaks are also attributed to hydrogen-bonded Ta−OH. The difference in the peak position may be due to a difference in the interlayer condition in the system created by nitridation. The small peak at 3.34 ppm of $H{-}Ca_2Ta_3O_{9.7}N_{0.2}{\cdot}xH_2O$ may be due to $Ta(2){-}NH_2$.

The structure of $CsCa_2Ta_3O_{10}$ belongs to the tetragonal P/mmm (D^1_{4h}) space group. The unit cell has 16 atoms so that the number of normal vibrations is 48. Employing Wyckoff site notation and factor group analysis, the complete vibrational representation of $CsCa_2Ta_3O_{10}$ can be described as follows:

$$\Gamma = 5A1g + B1g + 6Eg + 8A2u + 2B2u + 10Eu$$

where 5A1g + B1g + 6Eg are Raman active and 7A2u + 9Eu are IR active (1A2u + 1Eu are acoustic modes and 2B2u are silent modes). The Raman active modes, 5A1g + B1g + 6Eg, are related only to the motions of Ca (2 h site; Raman active mode: A1g + Eg), Ta(2) (2 g site; Raman active mode: A1g + Eg), O(2) (2 g site; Raman active mode: A1g + Eg), O(3) (4i site; Raman active mode: A1g + B1g + Eg), and O(4) (2 g site; Raman active mode: A1g + Eg) atoms; the Cs (1d site), Ta(1) (1a site), and O(1) (2f site) atoms do not directly contribute to Raman active modes according to group theory analysis. Thus, theory predicts that there will be 12 Raman-active modes and 16 IR-active modes.

However, the Raman spectrum for $CsCa_2Ta_3O_{10}$ contains at least 15 peaks (although some are small), which exceeds thenumber of theoretical Raman-active modes as shown in Figure 5a. The XRD analysis results indicate that the present material does not contain a detectable impurity phases (see SI). The oxygen atom sites in the crystal data ($CsCa_2Ta_3O_{10}$) refined from powder XRD patterns by Rietveld analysis[34] may differ from those of the actual material because it is generally difficult to accurately calculate the positions of oxygen atoms (i.e., light elements) in crystals from XRD patterns. Therefore, in the present study, the nitridation condition in the layered compound was analyzed not from the crystal data, but by comparing Raman spectra obtained before and after nitridation and proton exchange.

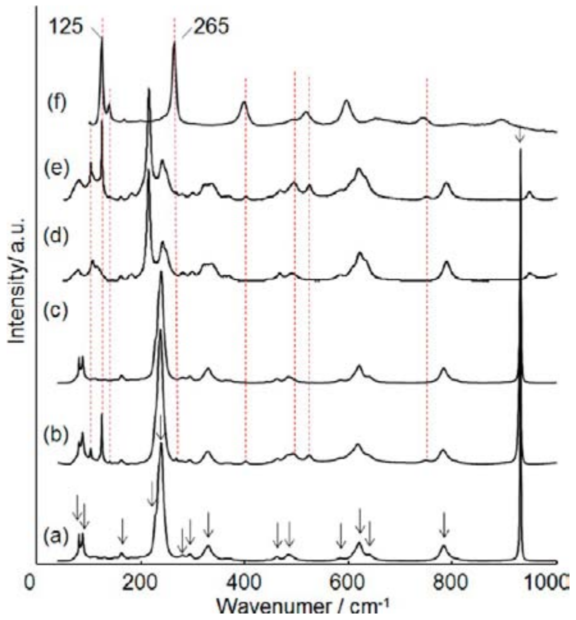

Figure 5. Raman spectra of (a) $CsCa_2Ta_3O_{10}$, (b) $CsCa_2Ta_3O_{9.7}N_{0.2}$, (c) $CsCa_2Ta_3O_{9.7}N_{0.2}$ calcinated at 800 °C in air, (d) $H-Ca_2Ta_3O_{10}$, and (e) $H-Ca_2Ta_3O_{9.7}N_{0.2}$, and (f) Ta_3N_5.

Figure 5a,b shows Raman spectra of $CsCa_2Ta_3O_{10}$ and $CsCa_2Ta_3O_{9.7}N_{0.2}$, respectively. Eight new peaks appear after nitridation (Figure 5b). When $CsCa_2Ta_3O_{9.7}N_{0.2}$ was calcinated at 800 °C, these eight peaks disappeared and the Raman spectrum became identical to that of the initial $CsCa_2Ta_3O_{10}$ (Figure 5c). This indicates that $CsCa_2Ta_3O_{9.7}N_{0.2}$ prepared by nitridation returns to the initial layered oxide by a reoxidation reaction. Figure 5d,e shows the Raman spectra obtained after proton exchange. In both the layered oxide and oxynitride spectra, the peak intensities at about 930 cm^{-1} decreased and shifted to higher wavenumber, the peaks at about 330 cm^{-1} split into two peaks at 300 and 335 cm^{-1}. Previous investigations of layered oxides $AAE_2Nb_3O_{10}{\cdot}xH_2O$ (A: Na, K, Rb, and Cs; AE: Ca, Sr, and Ba)[38] revealed that they have similar spectra to those of $CsCa_2Ta_3O_{10}$ and $CsCa_2Ta_3O_{9.7}N_{0.2}$. Based on comparison with the assignments for $AAE_2Ta_3O_{10}$, the Raman modes around 930 and 330 cm^{-1} were attributed to the vibration modes associated with the top oxygen atom, O(4), which is easily influenced by the interlayer species. In contrast, several peaks (including the above-mentioned eight new peaks) of layered oxynitride did not change on proton exchange. The eight peaks might be assigned to one of the following three kinds of vibrations: (1) those involving nitrogen atoms doped in the lattice; (2) those involving defects generated to compensate the charge balance after nitridation; and (3) those involving impurities phases. The Raman spectrum of Ta_3N_5 is shown in Figure 5(f), which matches fairly well with the eight new peaks described above. However, there is a slight difference in the positions and ratio of the two main peaks. The ratio of two main peak intensities at 125 and 265 cm^{-1} ($I_{265\ cm\text{-}1}/I_{125\ cm\text{-}1}$) in Ta_3N_5 was 0.96, while the two main peaks were at 125 and 268 cm^{-1} in $CsCa_2Ta_3O_{9.7}N_{0.2}$ with the ratio of 0.03 ($I_{268\ cm\text{-}1}/I_{125\ cm\text{-}1}$). The intensity of the peak at 268 cm^{-1} in $CsCa_2Ta_3O_{9.7}N_{0.2}$ was much weaker than that at 265 cm^{-1} in Ta_3N_5. In addition, some peaks such as at 595 and 900 cm^{-1} observed in Ta_3N_5 do not, however, clearly appear in $CsCa_2Ta_3O_{9.7}N_{0.2}$. Thus, the new eight peaks which appeared after the nitridation reaction cannot be assigned to Ta_3N_5. Furthermore, no Ta_3N_5 peaks were detected in the XRD patterns of $CsCa_2Ta_3O_{9.7}N_{0.2}$ (see SI Figure S1). These results suggest that the new eight peaks may not be due to an impurity phase, but may be associated with nitrogen atoms residing in the lattice, possibly converting a small portion of TaO_6 octahedra to $TaO_{6\text{-}x}N_x$ or TaN_6 octahedra in the layered compounds.

Exfoliation of layered $EA-Ca_2Ta_3O_{9.7}N_{0.2}$ to $Ca_2Ta_3O_{9.7}N_{0.2}$ nanosheets was confirmed by AFM observations. Figure 6a shows the appearance of a nanosheet suspension. The

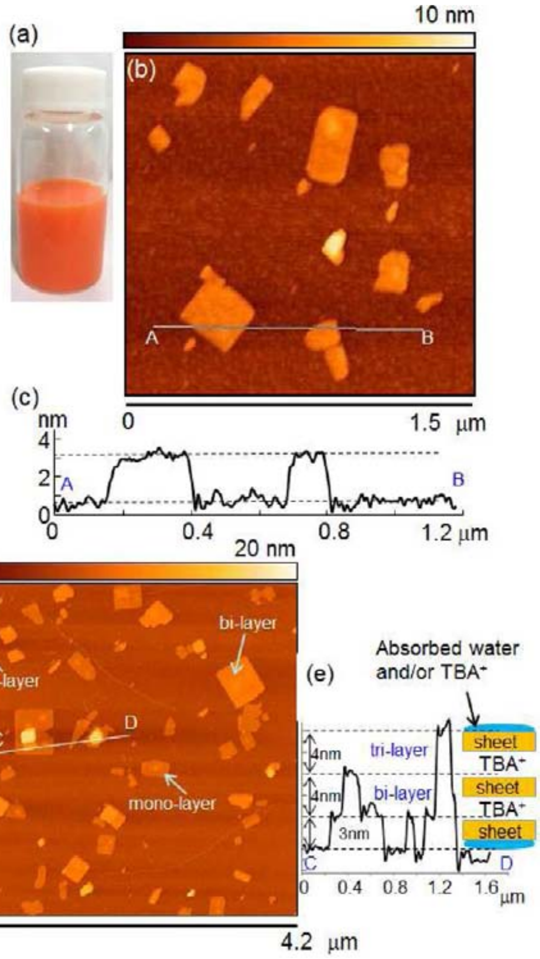

Figure 6. (a) The appearance of a nanosheet suspension, (b) AFM image and (c) cross-sectional profile of monolayer nanosheet, and (d) AFM image and (e) cross-sectional profile of bilayer and trilayer nanosheets.

suspension was orange in color due to nitrogen doping. Figure 6b shows an AFM image of $Ca_2Ta_3O_{9.7}N_{0.2}$ nanosheets. They had lateral dimensions of about 0.1−0.5 μm. Figure 6c shows a cross-sectional profile of a nanosheet measured between points A and B in Figure 6b. The nanosheets were approximately 2.8−3.1 nm thick, which is approximately 1.3 nm thicker than the theoretical perovskite blocks of the parent compound, estimated from crystallographic data. The difference between the nanosheet thickness estimated from AFM observations and the theoretically calculated thickness is due to the absorption of water and amine.[39] Furthermore, the nanosheet (liquid) suspension contained bilayer and trilayer nanosheets in addition to monolayer nanosheets, as shown in Figure 6d,e.

Figure 7a shows a TEM plan image of two oxynitride nanosheets. The square SAED pattern shown in Figure 7b confirms that the nanosheet has a single-crystal structure. Figure 7c shows a magnified TEM image of the nanosheet in Figure 7a. Lattice fringes are clearly observed over most of the observation area, except for at the edges (this may be because the edges were damaged during exfoliation). Figure 7d,e shows HAADF-STEM images of a nanosheet. The white spots are Ta atoms. The distance between neighboring Ta atoms is estimated to be 0.386 nm, which corresponds to an *a* axis length of 0.387 nm. For the sample shown in Figure 7d,e, the lattice fringes are obtained from the entire nanosheet. Thus, the nanosheet suspension consists of perfect single-crystal nanosheets and some nanosheets with damaged edges.

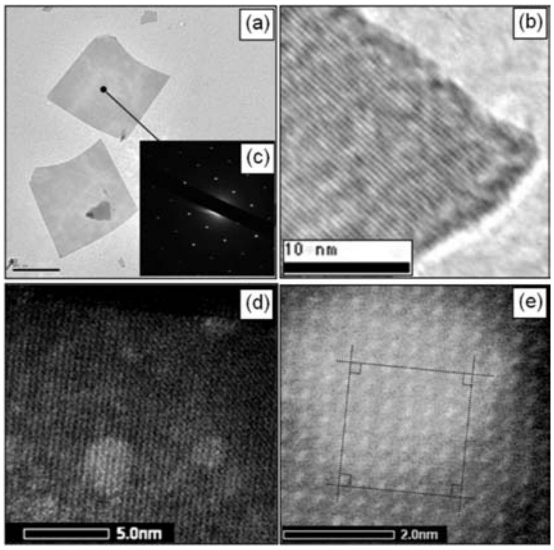

Figure 7. (a),(b) TEM images, (c) SAED pattern, and (d),(e) HAADF-STEM images of oxynitride nanosheets.

Figure 8a,b shows UV−vis spectra of the parent layered oxynitride, $CsCa_2Ta_3O_{9.7}N_{0.2}$, and the oxynitride nanosheet suspension, respectively. They contain two absorption bands: one around 500−600 nm and the other around 300−500 nm. The first absorption is due to excitation from the N 2p orbital to the Ta 5d orbital, while the second absorption band corresponds to excitation from the O 2p orbital to the Ta 5d orbital. The nanosheet and the parent compound had absorption edges at 597 and 582 nm, respectively. This decrease in the adsorption edge may be due to the quantum size effect that has been reported for exfoliation of layered parent oxides. In the visible light region, the light absorbance of the nanosheet suspension was weaker than that of $CsCa_2Ta_3O_{9.7}N_{0.2}$, which is due to the lower concentration of nanosheet suspension than that of the bulk materials. Figure 8c shows the absorption spectrum of nanosheet powder (solid) obtained by drying of the nanosheet suspension. The light absorbance of the nanosheet powder (solid) in the visible region was greater than that of the nanosheet suspension, but lower than the parent layered material. The ratio of nitrogen to oxygen in the nanosheet powder, measured by the HNO analysis, was almost the same as that of the parent layered material (2%). These results confirm that the oxynitride nanosheets did not decompose during the exfoliation reaction. Furthermore, the decrease in the absorbance in the visible light region might be due to some changes in the band structure of the materials before and after the exfoliation reaction. Figure 8d shows the UV−vis absorption spectrum for $CsCa_2Ta_3O_{10}$. The wavelength of the absorption edge (about 300 nm) was shorter than that of $CsCa_2Ta_3O_{9.7}N_{0.2}$.

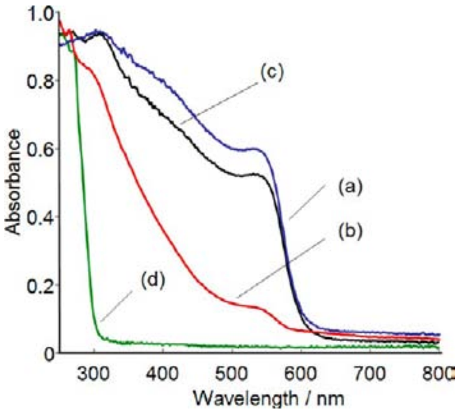

Figure 8. UV−vis absorption spectra of (a) $CsCa_2Ta_3O_{9.7}N_{0.2}$ and (b) $Ca_2Ta_3O_{9.7}N_{0.2}$ nanosheet suspension, (c) $Ca_2Ta_3O_{9.7}N_{0.2}$ nanosheet powder, and (d) $CaCa_2Ta_3O_{10}$.

Figure 9 shows XPS Ta 4d, Ta 4p and N 1s narrow spectra of Rh-loaded $Ca_2Ta_3O_{9.7}N_{0.2}$ nanosheet before and after the photocatalytic reaction for 24 h. The peaks at 241.2 and 230.1 eV were assigned to Ta(5+) $4d_{3/2}$ and $4d_{5/2}$, respectively. The binding energies of Ta $4p_{3/2}$ and N 1s peaks were observed at 403.9 and 395.6 eV, respectively. The peak at 395.6 eV was assigned to the Ta−N bond, indicating N doping within the nanosheet lattice. These energy positions in the XPS spectra

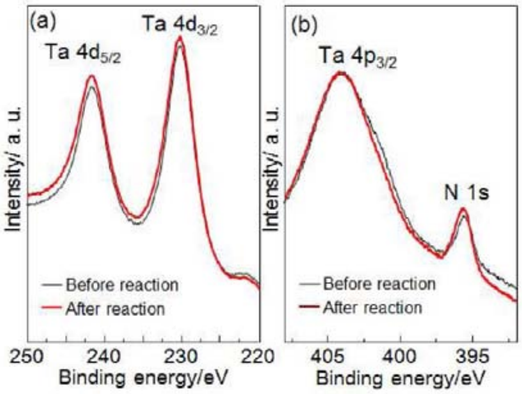

Figure 9. XPS narrow spectra of a Rh-loaded $Ca_2Ta_3O_{9.7}N_{0.2}$ nanosheet for (a) Ta $4d_{5/2}$ and $4d_{3/2}$ and (b) Ta $4p_{3/2}$ and N 1s before and after photocatalytic reaction for 24 h.

were constant before and after the photocatalytic reaction, indicating that $Ca_2Ta_3O_{9.7}N_{0.2}$ nanosheet is stable under photo irradiation.

Figure 10 shows the photocatalytic activity of oxynitride nanosheets. Figure 10a shows the effect of cocatalysts on H_2 production in a methanol aqueous solution under full arc irradiation. Methanol was employed as the sacrificial reagent. Nanosheets without a cocatalyst had a very low activity for photocatalytic hydrogen generation; the catalytic activity of the system with a cocatalyst was improved. In particular, Rh-loaded nanosheets exhibited the highest activity. The photocatalytic activity for H_2 production is plotted as a function of the amount of Rh loading in Figure 10b. The best performance was exhibited by 0.15 wt % Rh-loaded nanosheets. Figure 10c,d shows the amounts of H_2 and O_2, respectively, evolved under visible light (>420 nm) irradiation as a function of the irradiation time (Rh-loaded (0.15 wt %) $Ca_2Ta_3O_{9.7}N_{0.2}$ nanosheet). H_2 evolved from the system in aqueous methanol solutions, whereas O_2 evolved from the system in a 0.1 M $AgNO_3$ solution. These results indicate that Rh-loaded oxynitride nanosheets have the potential to decompose water into hydrogen and oxygen. Figure 10e,f shows the time dependence of hydrogen and oxygen evolution in pure water under full arc and visible light irradiation, respectively.

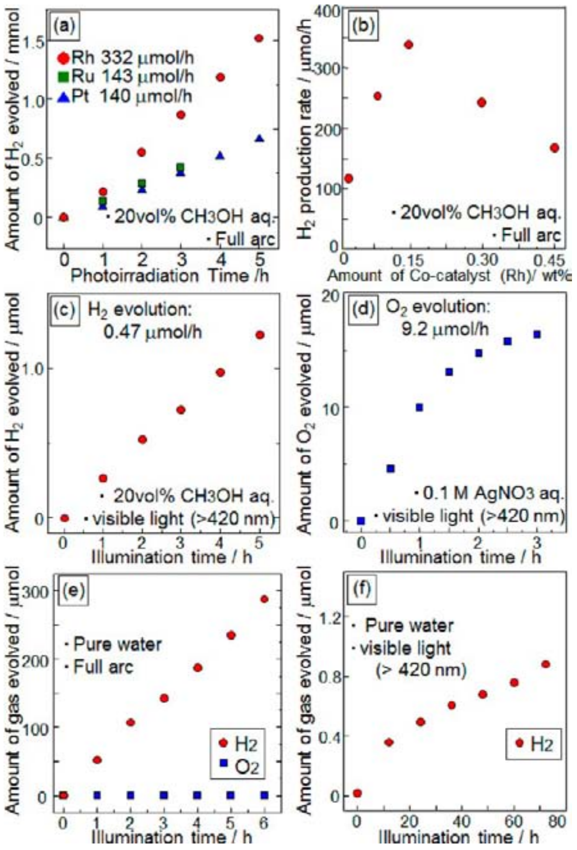

Figure 10. Photocatalytic activities of $CsCa_2Ta_3O_{9.7}N_{0.2}$ nanosheet; (a) the effect of cocatalysts on H_2 production in a 20 vol % methanol aqueous solution (loading amount: 0.15 wt%), (b) H_2 production as a function of the amount of Rh loading for 1 h, (c) H_2 evolved from a system in aqueous 20 vol % methanol solutions under visible light (>420 nm) irradiation, (d) O_2 evolved from the system in a 0.1 M $AgNO_3$ solution under visible light (>420 nm) irradiation, (e) H_2 and O_2 evolution from pure water under full arc, and (f) H_2 evolution from pure water under visible light irradiation. The amount of catalyst: 200 mg, catalyst: 0.15 wt % Rh-loaded samples.

The photocatalytic activity of the N-doped nanosheet for H_2 evolution under UV light in the presence of CH_3OH was relatively high (330 μmol/h), while the activity under visible light was low (0.47 μmol/h) as shown in Figure 10b and 10c. This implies that photoexcited electrons and holes in the nanosheet under the visible light irradiation easily recombine before the actual photo reaction. The possible reason for this recombination reaction might be the doping condition of nitrogen. There have been many studies on the effect of nitrogen doping in oxide semiconductors, such as N-doped TiO_2, on the photocatalytic reaction.[40−45] There are mainly two general understandings on the state of nitrogen doped into TiO_2, one understanding is that the states of N 2p for the substitutional nitrogen hybridize with O 2p states, and the other is that the substitutional nitrogen forms isolated N 2p states slightly above the O 2p valence band. These past studies reported decreases in the photoelectrochemical performance of N-doped TiO_2 electrodes in UV region, but enhancements in visible light region. The decrease in the photoelectrochemical performance is understood as due to the formation of isolated N 2p states above the O 2p valence band edge, which act as electron−hole recombination centers. In this present study, nitrogen doping created the visible light response for the photocatalytic reaction, although the catalytic activity was low. Thus, one of the possible reasons for the low photocatalytic activity of the N-doped $Ca_2Ta_3O_{9.7}N_{0.2}$ nanosheet in visible light region might be associated with the state of nitrogen doped into the lattice.

Figure 10e and 10f show the photocatalytic activity of Rh−loaded (0.15 wt.%) $Ca_2Ta_3O_{9.7}N_{0.2}$ nanosheets restacked with protons in pure water. Hydrogen was generated from pure water both under full arc and visible light irradiation, however there was no oxygen generated from this system. In order to investigate why oxygen was not generated in the photocatalytic reaction in pure water, products other than H_2, O_2, and N_2 were analyzed after the photocatalytic reaction in pure water. Small amounts of CH_4 and CH_3COO^- and $HCOO^-$ ions were detected from the gas and liquid phases, respectively.

These products may possibly have originated from TBA^+ and/or EA molecules utilized in the exfoliation and intercalation reactions. Figure 11a shows the IR spectrum of Rh-loaded nanosheet powder after washing with 0.1 M H_2SO_4. The small peaks at around 2800−3000 cm^{-1} are associated with the C−H stretching, suggesting that a small amount of organic

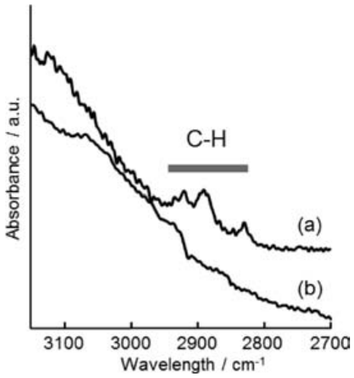

Figure 11. FT-IR spectra of Rh-loaded $Ca_2Ta_3O_{9.7}N_{0.2}$ nanosheet restacked with proton (a) before and (b) after photo irradiation.

amines might remain on the surface of nanosheets. Some organic amines may be strongly adsorbed onto the surface of nanosheets. This implies that the washing process was not sufficient to remove all the organic amines from the nanosheet surfaces.

It was, however, interesting to find that when the experiment was conducted over a longer period of time, oxygen was generated from the system (see SI Figure S4). In the period with no oxygen generation from the system, it is suspected that there are two main reactions occurring; the oxidation of organic amines and reduction of water into hydrogen. In the former reaction, the organic species absorbed on the nanosheet might get oxidized by holes. It is considered that this oxidation of organic species may be preventing the oxidation of water into oxygen, until all of the organic substances on the surface of catalysts is decomposed.

Figure 12 shows the photocatalytic hydrogen and oxygen generation of Rh-loaded (0.15 wt.%) $Ca_2Ta_3O_{9.7}N_{0.2}$ nanosheets restacked with protons under UV-light irradiation in pure water for 82 h, including the 42 h pretreatment of catalyst surfaces (Figure 12a). At 42 h since the start of the experiment, the amount of oxygen exceeded the corresponding amount of nitrogen (i.e., the ratio of oxygen to nitrogen became over 1/4). This implies that the oxidation of water became the preferential oxidation reaction of this system. Figure 12 (b) shows the photocatalytic hydrogen and oxygen generation after the pretreatment process (i.e., the amounts at 42 h are set as zero.) Both oxygen and hydrogen were generated, and the slopes for the amounts of hydrogen and oxygen evolved from the reaction remained constant for the next 40 h (42−82 h). The ratio of hydrogen to oxygen evolved was 3.1. These results indicate that the Rh-loaded $Ca_2Ta_3O_{9.7}N_{0.2}$ nanosheet is a potential catalyst for the photocatalytic splitting of water into hydrogen and oxygen. In addition, it was found that the removal of organic species such as organic amine from the surface of nanosheet was an essential process for initiating the water splitting reaction. The H_2/O_2 ratio differs from the theoretical value of 2. This might be associated with the products generated by photocatalytic decomposition reaction of organic species, which is currently being investigated. The ratio of nitrogen to oxygen in the nanosheet (2%) measured by the HNO analysis and the intensity of XPS signal at 395 eV (assigned to Ta−N bond) remained the same after the photocatalytic reaction, signifying that there was no decomposition of the catalyst during the reaction. This suggests that the present N-doped nanosheet is stable in the photocatalytic reaction. Further, the peak assigned to C−H bond in the IR spectrum disappeared after the photocatalytic reaction (Figure 11b), indicating that the organic species absorbed on nanosheet were decomposed during the photocatalytic reaction.

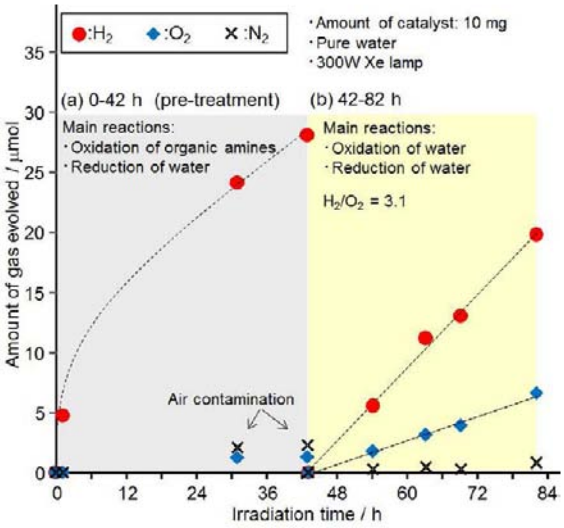

Figure 12. Time course of photocatalytic hydrogen and oxygen generation in pure water over Rh(0.15 wt %) loaded $Ca_2Ta_3O_{9.7}N_{0.2}$ nanosheets restacked with proton under UV-light irradiation (300 W Xe-lamp); (a) reaction period of 0−42 h, (b) 42−82 h. (It is noted that the amount of catalyst was reduced to 10 mg (c.f., 200 mg of catalyst used for the experiment in Figure 10e) in order to decompose the organic species absorbed on the nanosheet in a shorter period of time).

Figure 13 shows time courses of H_2 evolution from aqueous 20 vol % methanol solutions on photoirradiation (>400 nm) in the presence of 10 mg of $Ca_2Ta_3O_{9.7}N_{0.2}$ nanosheets, the protonated form of the nanosheets, and the parent layered oxynitride under full arc and visible light irradiation. All samples were loaded with Rh species by photodeposition. The H_2 production rates of the parent layered oxynitride ($CsCa_2Ta_3O_{9.7}N_{0.2}$) and protonated form ($H{-}Ca_2Ta_3O_{9.7}N_{0.2}$) were low under full arc irradiation, whereas the oxynitride nanosheet exhibited a high photocatalytic activity. The H_2 production rate of the nanosheets was 74 times greater than that of the parent layered oxynitride (Figure 13a). The H_2 production rate of the nanosheets under visible light irradiation was 33 times greater than that of the parent layered oxynitride as shown in Figure 13b. Since the present nanosheet suspension contains monolayer, bilayer, and trilayer nanosheets, this result does not represent the actual potential of monolayer nanosheets for photocatalytic hydrogen production. These results demonstrate that the improved photocatalytic activity originates from the characteristics of nanosheets such as their large surface areas, approximately 1-nm thickness, and high crystallinity. In addition, their slightly larger bandgap may contribute to their improved activity.

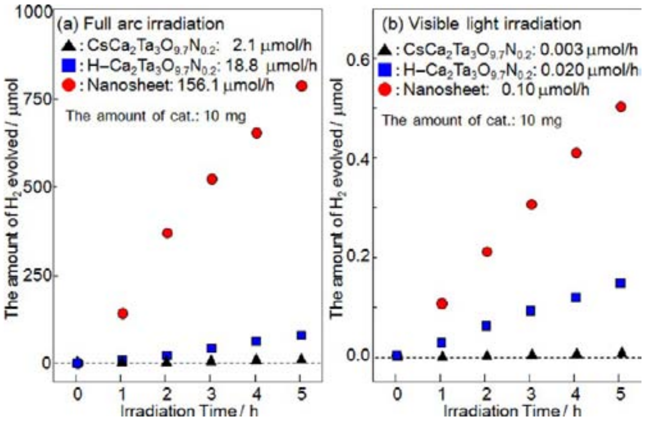

Figure 13. Time course of hydrogen evolution over $Ca_2Ta_3O_{9.7}N_{0.2}$ nanosheets, the protonated form of the nanosheets ($H{-}Ca_2Ta_3O_{9.7}N_{0.2}$), and the parent layered oxynitride ($CsCa_2Ta_3O_{9.7}N_{0.2}$) under (a) full arc irradiation and (b) visible light irradiation (>400 nm). The amount of catalyst: 10 mg, cocatalyst: 0.15 wt % Rh-loaded samples.

CONCLUSIONS

Tantalum-based oxynitride ($Ca_2Ta_3O_{9.7}N_{0.2}$) nanosheets were prepared for the first time from $CsCa_2Ta_3O_{9.7}N_{0.2}$ via proton exchange, EA intercalation, and exfoliation. The N/O molar ratio in $CsCa_2Ta_3O_{9.7}N_{0.2}$ was 2.4%. The nanosheets were approximately 2.8−3.1 nm thick, which is approximately 1.3 nm thicker than the theoretical perovskite blocks of the parent compound due to water and amine absorption. The nanosheet suspension contained bilayer and trilayer nanosheets in addition to monolayer nanosheets. Rh-loaded oxynitride nanosheets exhibited photocatalytic activity for H_2 and O_2 production from water under visible light irradiation in the presence of sacrificial agents. In contrast, the parent layered oxynitride, $CsCa_2Ta_3O_{9.7}N_{0.2}$, exhibited very low photocatalytic activity. Further, Rh-loaded (0.15 wt %) $CsCa_2Ta_3O_{9.7}N_{0.2}$ nanosheet exhibited activity for H_2 and O_2 evolution from pure water under UV-light irradiation. The ratio of hydrogen to oxygen evolved was around 3. The present N-doped nanosheet is stable during the photocatalytic reaction. The present results demonstrate the potential application of oxynitride nanosheets for photocatalytic H_2 production from water.

ASSOCIATED CONTENT

Ⓢ Supporting Information

XRD pattern (S1, S2), apparatus for photocatalytic reaction (S3), and the time course of photocatalytic hydrogen and oxygen generation in pure water over Rh(0.15 wt.%) loaded $Ca_2Ta_3O_{9.7}N_{0.2}$ nanosheets under UV-light irradiation (S4). This material is available free of charge via the Internet at http://pubs.acs.org.

AUTHOR INFORMATION

Corresponding Author

s-ida@cstf.kyushu-u.ac.jp

Notes

The authors declare no competing financial interest.

ACKNOWLEDGMENTS

This work was supported by JST PRESTO program.

REFERENCES

(1) Sasaki, T.; Watanabe, M.; Hashizume, H.; Yamada, H.; Nakazawa, H. *J. Am. Chem. Soc.* **1996**, 8329−8335.

(2) Kudo, A.; Tanaka, A.; Domen, K.; Maruya, K.; Aika, K.; Onishi, T. *J. Catal.* **1988**, *111*, 67−76.

(3) (a) Schaak, R. E.; Mallouk, T. E. *Chem. Mater.* **2000**, *12*, 2513−2516. (b) Schaak, R. E.; Mallouk, T. E. *Chem. Mater.* **2000**, *12*, 3427−3434. (c) Schaak, R. E.; Mallouk, T. E. *Chem. Commun.* **2002**, 706−707.

(4) Han, Y.-S.; Park, I.; Choy, J.-H. *J. Mater. Chem.* **2001**, *11*, 1277−1282.

(5) Sugimoto, W.; Tarabayashi, O.; Murakami, Y.; Takasu, Y. *J. Mater. Chem.* **2002**, *12*, 3814−3818.

(6) Takagaki, A.; Lu, D.; Kondo, J. N.; Hara, M.; Hayashi, S.; Domen, K. *Chem. Mater.* **2005**, *17*, 2487−2489.

(7) Abe, R.; Shinohara, K.; Tanaka, A.; Hara, M.; Kondo, J. N.; Domen, K. *J. Mater. Res.* **1998**, *13*, 861−865.

(8) Omomo, Y.; Sasaki, T.; Wang, L. Z.; Watanabe, M. *J. Am. Chem. Soc.* **2003**, *125*, 3568−3575.

(9) (a) Ida, S.; Ogata, C.; Unal, U.; Izawa, K.; Inoue, T.; Altuntasoglu, O.; Matsumoto, Y. *J. Am. Chem. Soc.* **2007**, *129*, 8956−8957. (b) Ida, S.; Ogata, C.; Eguchi, M.; Youngblood, W. J.; Mallouk, T. E.; Matsumoto, Y. *J. Am. Chem. Soc.* **2008**, *130*, 7052−7059.

(10) Ozawa, T. C.; Fukuda, K.; Akatsuka, K.; Ebina, Y.; Sasaki, T. *Chem. Mater.* **2007**, *19*, 6575−6580.

(11) Nadeau, P. H.; Wilson, M. J.; McHardy, W. J.; Tait, J. M. *Science* **1984**, *225*, 923.

(12) (a) Adachi-Pagano, M.; Forano, C.; Besse, J.-P. *Chem. Commun.* **2000**, 91−92. (b) Leroux, F.; Adachi-Pagano, M.; Intissar, M.; Chauvière, S.; Forano, C.; Besse, J.-P. *J. Mater. Chem.* **2001**, *11*, 105−112.

(13) (a) Ma, R.; Liu, Z.; Takada, K.; Iyi, N.; Bando, Y.; Sasaki, T. *J. Am. Chem. Soc.* **2007**, *129*, 5257−5263. (b) Ma, R.; Takada, K.; Fukuda, K.; Iyi, N.; Bando, Y.; Sasaki, T. *Angew. Chem., Int. Ed.* **2008**, *47*, 86−89.

(14) (a) Ida, S.; Shiga, D.; Koinuma, M.; Matsumoto, Y. *J. Am. Chem. Soc.* **2008**, *130*, 14038−14039. (b) Ida, S; Sonoda, Y, Yuki; Ikeue, K; Matsumoto, Y *Chem. Commun.* **2010**, *46*, 877−879.

(15) Novoselov, K. S.; Geim, A. K.; Morozov, S. V.; Jiang, D.; Zhang, Y.; Dubonos, S. V.; Grigorieva, I. V.; Firsov, A. A. *Science* **2004**, *306*, 666−669.

(16) Usuki, A.; Kojima, Y.; Kawasumi, M.; Okada, A.; Fukushima, Y.; Kurauchi, T.; Kamigaito, O. *J. Mat. Res.* **1993**, *8*, 1179.

(17) Lopez-Galindo, A.; Viseras, C.; Cerezo, P. *Appl. Clay Sci.* **2007**, *36*, 51−63.

(18) Lin, Y.-M.; Dimitrakopoulos, C.; Jenkins, K. A.; Farmer, D. B.; Chiu, H.-Y.; Grill, A.; Avouris, Ph. *Science* **2010**, *327*, 662.

(19) Liu, G.; Wang, L.; Sun, C.; Chen, Z.; Yan, X.; Cheng, L.; Cheng, H.-M.; Lu, G Q. *Chem. Commun.* **2009**, 1383−1385.

(20) Matsumoto, Y.; Koinuma, M.; Iwanaga, Y.; Sato, T.; Ida, S. *J. Am. Chem. Soc.* **2009**, *131*, 6644−6645.

(21) Maeda, K.; Teramura, K.; Lu, D.; Takata, T.; Saito, N.; Inoue, Y.; Domen, K. *Nature* **2006**, *440*, 295.

(22) Hitoki, G.; Takata, T.; Kondo, J. N.; Hara, M.; Kobayashi, H.; Domen, K. *Chem. Commun.* **2002**, 1698−1699.

(23) Higashi, M.; Abe, R.; Teramura, K.; Takata, T.; Ohtani, B.; Domen, K. *Chem. Phys. Lett.* **2008**, *452*, 120−123.

(24) Zong, X.; Sun, C.; Chen, Z.; Mukherji, A.; Wu, H.; Zou, J.; Smith, S. C.; Lu, G. Q.; Wang, L. *Chem. Commun.* **2011**, *47*, 6293−6295.

(25) Kim, Y.-I.; Woodward, P. M.; Baba-Kishi, K. Z.; Tai, C. W. *Chem. Mater.* **2004**, *16*, 1267−1276.

(26) Zhang, Y.-R.; Motohashi, T.; Masubuchi, Y.; Kikkawa, S. *J. Ceram. Soc. Jpn.* **2011**, *119*, 581−586.

(27) Kikuchi, A.; Ishihara, A.; Matsuzawa, K.; Mitsushima, S.; Ota, K. *Chem. Lett.* **2009**, *38*, 1184−1185.

(28) Abe, R.; Shinohara, K.; Tanaka, A.; Hara, M.; Kondo, J. N.; Domen, K. *Chem. Mater.* **1997**, *9*, 2179−2184.

(29) Hata, H.; Kobayashi, Y.; Bojan, V.; Youngblood, W. J.; Mallouk, T. E. *Nano Lett.* **2008**, *8*, 794−799.

(30) (a) Ebina, Y.; Sasaki, T.; Harada, M.; Watanabe, M. *Chem. Mater.* **2002**, *14*, 4390−4395. (b) Ebina, Y.; Sakai, N.; Sasaki, T. *J. Phys. Chem. B* **2005**, *109*, 17212−17216.

(31) (a) Comptons, O. C.; Mullet, C. H.; Chiang, S.; Osterloh, F. E. *J. Phys. Chem. C* **2008**, *112*, 6202−6208. (b) Townsend, T. K.; Sabio, E. M.; Browning, N. D.; Osterloh, F. E. *ChemSusChem* **2011**, *4*, 185−190.

(32) Maeda, K.; Mallouk, T. E. *J. Mater. Chem.* **2009**, *19*, 4813−4818.

(33) Okamoto, Y.; Ida, S.; Hyodo, J.; Hagiwara, H.; Ishihara, T. *J. Am. Chem. Soc.* **2011**, *133*, 18034−18037.

(34) Toda, K.; Teranishi, T.; Ye, Z.-G.; Sato, M.; Hinatsu, Y. *Mater. Res. Bull.* **1999**, *34*, 971−982.

(35) Takagaki, A.; Sugisawa, M.; Lu, D.; Kondo, J. N.; Hara, M.; Domen, K.; Hayashi, S. *J. Am. Chem. Soc.* **2003**, *125*, 5479−5485.

(36) (a) Takagaki, A.; Yoshida, T.; Lu, D.; Kondo, J. N.; Hara, M.; Domen, K.; Hayashi, S. *J. Phys. Chem. B* **2004**, *108*, 11549−11555. (b) Takagaki, A.; Lu, D.; Kondo, J. N.; Hara, M.; Hayashi, S.; Domen, K. *Chem. Mater.* **2005**, *17*, 2487−2489. (c) Tagusagawa, C.; Takagaki, A.; Hayashi, S.; Domen, K. *J. Phys. Chem. C* **2009**, *113*, 7831−7837.

(37) Avenier, P.; Lesage, A.; Taoufik, M.; Baudouin, A.; Mallmann, A. D.; Fiddy, S.; Vautier, M.; Veyre, L.; Basset, J.-M.; Emsley, L.; Quadrelli, E. A. *J. Am. Chem. Soc.* **2007**, *129*, 176−186.

(38) Byeon, S.-H.; Nam, H.-J. *Chem. Mater.* **2000**, *12*, 1771−1778.

(39) (a) Izawa, K.; Yamada, T.; Unal, U.; Ida, S.; Altuntasoglu, O.; Koinuma, M.; Matsumoto, Y. *J. Phys. Chem. B* **2006**, *110*, 4645−4650. (b) Fukuda, K.; Nakai, I.; Ebina, Y.; Tanaka, M.; Mori, T.; Sasaki, T. *J. Phys. Chem. B* **2006**, *110*, 17070−17075.

(40) Asahi, R.; Morikawa, T.; Ohwaki, T.; Aoki, K.; Taga, Y. *Science* **2001**, *293*, 269−271.

(41) Beranek, R.; Neumann, B.; Sakthivel, S.; Janczarek, M.; Dittrich, T.; Tributsch, H.; Kisch, H. *Chem. Phys.* **2007**, *339*, 11−19.

(42) Nakamura, R.; Tanaka, T.; Nakato, Y. *J. Phys. Chem. B* **2004**, *108*, 10617−10620.

(43) Torres, G. R.; Lindgren, T.; Lu, J.; Granqvist, C. G.; Lindquist, S. E. J *J. Phys. Chem. B* **2004**, *108*, 5995−6003.

(44) Lindgren, T.; Lu, J.; Hoel, A.; Granqvist, C. G.; Torres, G. R.; Lindquist, S. E. *Sol. Energy Mater. Sol. Cells* **2004**, *84*, 145−157.

(45) Hoang, S.; Guo, S.; Hahn, N. T.; Bard, A. J.; Mullins, C. B. *Nano Lett.* **2012**, *12*, 26−32.